galaxies

MDPI

Article

Ba Isotope Ratio in CEMP-s and CEMP-rs Stars as a Signature of s-Process and i-Process

Tatyana Sitnova * and Lyudmila Mashonkina

Institute of Astronomy, Russian Academy of Sciences, Moscow 119017, Russia; lima@inasan.ru
* Correspondence: sitamih@gmail.com

Abstract

We present a spectroscopic analysis of three carbon-enhanced metal-poor (CEMP) stars of type CEMP-s and CEMP-rs and determine their non-local thermodynamic equilibrium (NLTE) abundances of Ba and the fractions of the odd Ba isotopes (F_{odd}). We found $F_{odd} = 0.65^{+0.35}_{-0.34}$ in SDSS J1349-0229, which is known in the literature as a CEMP-rs star, while the other two stars, BPS CS 29512-073 and SDSS J1036+1212, exhibit lower $F_{odd} = 0.23^{+0.19}_{-0.10}$ and $0.23^{+0.22}_{-0.11}$, respectively, and they are known in the literature as CEMP-s stars. The present result supports our earlier finding about distinct F_{odd} in CEMP-s and CEMP-rs stars. For obtaining observational constraints on i-process nucleosynthesis, further NLTE abundance determinations for many chemical elements are required.

Keywords: CEMP-s stars; CEMP-rs stars; s-process; i-process; high-resolution spectroscopy; abundances; isotope ratios

1. Introduction

Neutron (n) capture processes may occur at different conditions and, depending on the neutron flux, are classified as slow (s), rapid (r), and intermediate (i) processes [1,2]. In this study, we focus on obtaining observational constraints for s- and i-process nucleosynthesis. The main s-process operates in low- and intermediate-mass stars during the asymptotic giant branch (AGB) evolutionary stage [3,4]. For the i-process, specific conditions, such as proton ingestions into a He-burning zone, need to occur for producing higher neutron densities than those typical of the s-process. The supposed i-process sites are metal-poor (MP) AGB stars [5–8] and accreting white dwarfs [9]. The main observational signature of the s-process is an enhanced Ba abundance, while the i-process is predicted to produce a significant overabundance of Eu in addition to Ba.

Ba is considered an s-element, as 88% of the solar Ba originates from the s-process, while Eu is referred to as an r-element, with 95% of the solar Eu originating from the r-process [10]. These properties led to the classification of carbon-enhanced metal-poor (CEMP) stars with enhanced abundances of n-capture elements as CEMP-s and CEMP-rs stars, which trace the s- and i-process, respectively. These stars are members of binary systems [11–13] and they were enriched by material transferred from their companion stars, which have since evolved into white dwarfs. The chemical composition of the CEMP-s,rs stars is important for constraining the s- and i-process nucleosynthesis. While the s-process is well studied and used in galactic chemical evolution modeling, the i-process is less well understood.

To study the i-process, it is first necessary to identify stars that trace i-process nucleosynthesis. Such stars are expected to show radial velocity variations, as well as enhanced

Check for updates

Academic Editors: Sergio Cristallo, Luciano Piersanti and Diego Vescovi

Received: 26 February 2026
Revised: 27 April 2026
Accepted: 29 April 2026
Published: 6 May 2026

Copyright: © 2026 by the authors. Licensee MDPI, Basel, Switzerland. This article is an open access article distributed under the terms and conditions of the Creative Commons Attribution (CC BY) license.

C, Ba, and Eu abundances. Several criteria have been proposed to distinguish CEMP-rs stars from CEMP-s stars, and some of them are listed in Table 1. These criteria are largely formal, and in practice stars rarely fall clearly into distinct categories.

Table 1. Classification schemes available in the literature for distinguishing between CEMP-s and CEMP-rs stars.

s	rs	Ref.
[Ba/Eu] > 0.5	$0.0 <$ [Ba/Eu] < 0.5	[14]
[Ba/Fe] > 1.0, [Eu/Fe] < 1, [Ba/Eu] > 0	[Ba/Fe] > 1.0, [Eu/Fe] > 1, [Ba/Eu] > 0	[15]
[Ba/Fe] > 1.0, [Ba/Eu] > 0	[Ba/Fe] > 1.0, [Eu/Fe] > 1, [Ba/Eu] > 0	[16]
[Ba/Fe] > 0, $-0.5 <$ [Sr/Ba] < 0.8	[Ba/Fe] > 0, $-1.5 <$ [Sr/Ba] < -0.5	[17]
[La/Eu] > 0.5	$0 <$ [La/Eu] < 0.5	[18]
[Ba/Fe] > 1.0 and [Eu/Fe] < 1, [Ba/Eu] > 0 and/or [La/Eu] > 0.5 or [Eu/Fe] > 1.0, [Ba/Eu] > 1.0 and/or [La/Eu] > 0.7	[Ba/Fe] > 1.0, [Eu/Fe] > 1 and $0 <$ [Ba/Eu] < 1 and/or $0.0 <$ [La/Eu] < 0.7	[19]

Different studies may classify the same star as a CEMP-s or a CEMP-rs star. For one of the most extensively studied CEMP stars, namely, HD 196944 [18,20–28], its chemical composition has been investigated in numerous papers using high-resolution and high signal-to-noise (S/N) spectra obtained with many spectrographs/telescopes, including the UVES/VLT, CASPEC and HARPS/3.6 m ESO telescope, HERMES/1.2 m Mercator telescope, HDS/Subaru, MIKE/Magellan, STIS/HST, and 2dCoude echelle spectrograph/2.7 m Harlan J. Smith Telescope at McDonald Observatory. Despite the numerous observations available, the origin of the neutron-capture element overabundances in HD 196944 remains unclear, and there is no consensus on whether this star should be classified as CEMP-s [28,29] or CEMP-rs [18,30]. This disagreement is not surprising, as different studies report significantly different [Ba/Eu][1] abundance ratios for HD 196944, ranging from 1.10 [28] to 0.24 [18]. Table 2 summarizes the stellar atmosphere parameters, as well as the [Ba/Fe], [Eu/Fe], and [Ba/Eu] abundance ratios derived by different authors. In addition to differences in observational data and adopted stellar parameters, abundance determinations are also affected by different treatments of line formation, whether under the local thermodynamic equilibrium (LTE) assumption or taking departures from LTE (i.e., NLTE effects) into account. NLTE leads to higher Eu abundance but lower Ba abundances from the Ba II subordinate lines, resulting in a shift in [Ba/Eu] from 0.84 in LTE to 0.39 in NLTE in the case of HD 196944 [30].

Table 2. Literature data on HD 196944.

$T_{\rm eff}$/log g/$\xi_{\rm t}$	[Fe/H]	[Ba/H]	[Ba/Fe]	[Eu/H]	[Eu/Fe]	[Ba/Eu]	Note	Class.	Ref.
5390/2.13/2.0	−2.21	−1.36	0.85	−1.75	0.46	0.39	NLTE	rs	[30]
	−2.21	−1.03	1.18	−1.87	0.34	0.84	LTE	rs	[30]
5428/2.11/1.7	−2.09	−0.86	1.23	−1.96	0.13	1.10	LTE	s	[28]
5158/1.28/1.7	−2.50	−1.48	1.02	−2.00	0.50	0.52	LTE	rs	[18]
	−2.50	-	-	−1.72	0.78	0.24	NLTE: Eu, LTE: Ba	rs	[18]
5250/1.80/1.7	−2.25	−1.15	1.10	−2.08	0.17	0.93	LTE	s	[22]
5353/1.70/1.9	−2.23	−1.09	1.14	-	-	-	-		[23]
5250/1.70/1.9	−2.45	−0.89	1.56	-	-	-	-		[20]

A more robust classification method for CEMP-s and CEMP-rs stars, which uses additional heavy elements beyond Ba and Eu, has been proposed by Karinkuzhi et al. [18]. This approach is based on a comparison of stellar abundance patterns with the solar scaled

r-process pattern. This method implies that CEMP-rs stars match the solar scaled r-process pattern better than CEMP-s stars.

In the search for a more physically motivated, rather than phenomenological, approach to distinguishing i-process and s-process tracers, Van Eck et al. [31] suggested using the Ba isotope ratio. In stars, Ba can be represented by five isotopes: ^{134}Ba, ^{135}Ba, ^{136}Ba, ^{137}Ba, and ^{138}Ba. The isotopes ^{134}Ba and ^{136}Ba are s-only isotopes and cannot be produced in r- and i-processes due to the presence of stable r-only isotopes ^{134}Xe and ^{136}Xe, which block the β-decay pathway and prevent the formation of ^{134}Ba and ^{136}Ba. Therefore, different fractions of odd Ba isotopes (F_{odd} = (N(^{135}Ba) + N(^{137}Ba))/N(Ba)) are predicted for the s-process: F_{odd} = 0.10 [10] and for the i-process: F_{odd} = 0.60 to 0.80 [32]. This idea is clear and reasonable, and the only limitation lies in methodological challenges arising from strong saturation of the Ba II resonance lines and blending with molecular carbon lines in CEMP stars, which obstructs accurate analysis of the Ba II resonance lines.

For determination of the Ba isotope ratio, CEMP stars with high T_{eff} and log g are better suited than cool giants, as molecular carbon lines are weak or absent and the Ba II resonance lines are much less saturated. Sitnova et al. [30] determined F_{odd} in nine hot CEMP-s and CEMP-rs stars with the Ba II resonance lines equivalent widths (EW) of less than 185 mÅ. It has been shown that, indeed, different CEMP stars have distinct Ba isotope ratios.

The number of stars available for this kind of analysis remains very small, and, unfortunately, Sitnova et al. [30] overlooked three CEMP stars that have Ba II resonance lines suitable for F_{odd} determinations. These stars are SDSS J1349-0229 and SDSS J1036+1212, which were classified as CEMP-rs and CEMP-s, respectively, by Behara et al. [33], and BPS CS 29512-073, which was classified as CEMP-s by Allen et al. [34]. All three stars were recently analyzed by Riyas et al. [35], who confirmed their classification from the literature. In this study we aim to determine F_{odd} in these three stars and to check whether the derived values are consistent with the literature classification.

The paper is structured as follows. In Section 2 we describe our sample stars, observations, and stellar atmosphere parameters. The abundance determination method is presented in Section 3. We discuss our findings in Section 4, and we summarize our conclusions in Section 5.

2. Stellar Sample, Observations, and Atmospheric Parameters

All three stars were analyzed by Riyas et al. [35], who classified SDSS J1349-0229 as a CEMP-rs star and BPS CS 29512-073 and SDSS J1036+1212 as CEMP-s stars by determining their detailed chemical abundance patterns. We checked all the 17 stars from Riyas et al. [35] and found that only three stars meet our selection criteria for the Ba II resonance lines not being too saturated for Ba isotope ratio analysis.

We used high-resolution spectra from the UV-Visual Echelle Spectrograph (UVES) at the UT2 Kueyen Telescope that are available in the European Southern Observatory Science Archive[2]. The quality of the adopted spectra is reasonable, with a spectral resolving power of $\lambda/\Delta\lambda > 30{,}000$ and a S/N per pixel of >30. The program IDs and the characteristics of the observed spectra are listed in Table 3.

Stellar atmosphere parameters were determined using Gaia photometry and parallaxes, as well as the NLTE abundances from Fe I and Fe II lines. We calculated the effective temperatures (T_{eff}) using the *Gaia* BP − G, G − RP, BP − RP dereddened colors and the calibration of Mucciarelli et al. [36]. The extinction E(B − V) was adopted from Green et al. [37], and the colors were corrected according to Casagrande and VandenBerg [38]. Different colors yield very similar effective temperatures, and the uncertainty in T_{eff} is therefore mainly defined by an uncertainty in the calibration of 80 K as given by Mucciarelli et al. [36].

Table 3. Stellar sample, atmospheric parameters, and characteristics of the observed spectra.

Name, Type	E(B−V)	$T_{\rm eff}$, K	log g *, cm s^{-2}	[Fe/H]	$\xi_{\rm t}$, km s^{-1}	S/N$_{\rm red}$	R, 10^3	Program ID
SDSS J1349-0229, rs	0.05	6150	4.28 (0.12)	−2.84 (0.10)	1.2	70	31	078.D-0217(A), 383.D-0927(A)
SDSS J1036+1212, s	0.02	5720	3.47 (0.10)	−3.27 (0.12)	1.3	62	31	078.D-0217(A)
BPS CS 29512-073, s	0.04	5760	3.65 (0.10)	−1.88 (0.03)	1.3	125	42	076.D-0451(A)

Note. *—The log g and [Fe/H] uncertainties are indicated in parentheses. For each sample star, the uncertainties in $T_{\rm eff}$ and $\xi_{\rm t}$ of 80 K and 0.1 km s^{-1}, respectively, were adopted.

We calculated the surface gravities (log g) using distances based on *Gaia* parallaxes. The parallaxes were corrected for the zero offset according to Lindegren et al. [39], and the distances were computed from the maximum of the probability distribution function as described by Bailer-Jones [40]. With these distances, effective temperatures, bolometric corrections of Casagrande and VandenBerg [38], and assuming a mass of 0.8 solar masses, we derived the surface gravities using the formula $\log g = 4.44 + \log(m/m_{\odot}) + 0.4(M_{\rm bol} - 4.75) + 4\log(T_{\rm eff}/5780)$, where $m_{\odot}$ is the solar mass, and $M_{\rm bol}$ is the absolute bolometric magnitude.

The most metal-rich sample star BPS CS 29512-073 has the observed spectrum with the highest S/N ratio compared to the other two sample stars. Therefore, in BPS CS 29512-073 we determined iron abundances from 49 lines of Fe I and 8 lines of Fe II. For the lines of Fe I, we applied the NLTE abundance corrections from Mashonkina et al. [41], which are available in the INASAN database[3] [42]. The NLTE effects for the Fe II lines are negligible in the stellar parameter range we considered [41,43]. When applying a 50 K lower $T_{\rm eff}$ and 0.1 dex lower log g compared to those derived for BPS CS 29512-073 from photometry, we found consistent within the error bars NLTE abundances from Fe I and Fe II, with the average values of $\log\varepsilon$ = 5.53[4] ± 0.08 and 5.57 ± 0.03, respectively. These stellar parameters are presented in Table 3. Iron abundances from individual lines with their atomic data are given in Table A1.

When applying the same list of iron lines to the two other sample stars, we detected only five lines of Fe I and Fe II (Table A1). In SDSS J1036+1212, we found $\log\varepsilon$ (Fe I) = 4.33 ± 0.11 and $\log\varepsilon$ (Fe II) = 4.18 ± 0.10 in NLTE, when using photometric $T_{\rm eff}$ and log g. In SDSS J1349-0229, we applied 70 K lower $T_{\rm eff}$ and 0.12 dex higher log g compared to those derived from photometry, and found in NLTE $\log\varepsilon$ (Fe I) = 4.74 ± 0.07 and $\log\varepsilon$ (Fe II) = 4.61 ± 0.10. In these two stars, the small number of iron lines and their small EWs prevented us from further tuning the stellar parameters for obtaining a perfect match between NLTE abundances from Fe I and Fe II. The microturbulent velocity was computed using an empirical relation based on NLTE analysis of Fe I and Fe II lines in dwarfs [44].

We compared our stellar atmosphere parameters with those derived in the original studies of the sample stars. Behara et al. [33] determined the effective temperatures from the wings of the Hα line and the Fe I excitation equilibrium. The surface gravity was derived from the Fe I/Fe II ionization equilibrium. For SDSS J1349-0229 they found $T_{\rm eff}$/log g = 6200 K/4.0. $T_{\rm eff}$ is consistent within the error bars with our determinations of 6150 K ± 80 K, while we found a higher log g = 4.28 ± 0.12. For SDSS J1036+1212 Behara et al. [33] determined $T_{\rm eff}$/log g = 6000 K/4.0, while we found significantly lower $T_{\rm eff}$ = 5720 K ± 80 K and log g = 3.47 ± 0.10. It is known that the effective temperatures derived from the Fe I excitation equilibrium are systematically, by up to several hundred K, lower compared to those derived from photometry [45,46] and underestimated $T_{\rm eff}$ results in an underestimated log g when determined from the Fe I/Fe II ionization equilibrium. For SDSS J1036+1212 the situation is the opposite and it can hardly be understood. We attribute

this discrepancy to a large uncertainty in Behara et al. [33] determinations caused by evaluating stellar parameters from a small number of weak iron lines in SDSS J1036+1212.

While an accurate analysis of the Balmer line wings is beyond the scope of the present study, for illustration, we plot the Hα line profiles in the sample stars together with their 1D LTE synthetic spectra computed with $T_{\rm eff}$/log g/[Fe/H] = 5720 K/3.47/−3.3 and 6150 K/4.28/−2.8 and representing SDSS J1036+1212 and SDSS J1349-0229, respectively (Figure A1). Figure A1 demonstrates that SDSS J1036+1212 is significantly cooler than SDSS J1349-0229, and its temperature is very close to that of BPS CS 29512-073, in line with our determination of $T_{\rm eff}$ = 5720 K ± 80 K.

For BPS CS 29512-073 Allen et al. [34] determined $T_{\rm eff}$/log g = 5560 K ± 50 K/3.44 ± 0.07 using an iterative process that employs photometric $T_{\rm eff}$ and log g from isochrones as a first step, and then revised them using Fe I excitation equilibrium and Fe I/Fe II ionization balance in LTE. We found $T_{\rm eff}$ = 5760 K ± 80 K and log g = 3.65 ± 0.10, supporting the idea that the effective temperatures derived from the Fe I excitation equilibrium are systematically lower compared to those derived from photometry. The Hα line wings also support the adopted $T_{\rm eff}$ (Figure A1).

3. Abundance Analysis

The line list was extracted from the Vienna Atomic Line Database VALD [47,48], which includes isotopic and hyperfine splitting (HFS). For Ba II lines, VALD provides the oscillator strengths (log gf) from Miles and Wiese [49]. We compared these log gf with the most recent laboratory results of De Munshi et al. [50] for the Ba II 4934 Å and 6496 Å and Dutta et al. [51] for the Ba II 4554 Å, 5853 Å, and 6141 Å, where the branching factors were measured with an accuracy of better than one percent. The differences in log gf values between the recent measurements and those from Miles and Wiese [49] amounts to 0.00, −0.02, −0.02, 0.01, and 0.01 for the Ba II 4554 Å, 4934 Å, 5853 Å, 6141 Å, and 6496 Å, respectively. In this study, we used the oscillator strengths for Ba II lines from De Munshi et al. [50] and Dutta et al. [51]. For consistency, for our comparison sample stars from Sitnova et al. [30], we recomputed barium abundances and $F_{\rm odd}$ using the same log gf values. The oscillator strengths for Eu II lines were taken from the laboratory measurements of Lawler et al. [52]. The HFS components for the Ba II lines were taken from Wendt et al. [53] and for the Eu II lines from Hühnermann et al. [54], Möller et al. [55], and Revalde et al. [56]. We present the list of isotopic and HFS components of the Ba II and Eu II lines in Tables A2 and A3, respectively. We provide a tool for generating the lists of Ba II lines for a given $F_{\rm odd}$ and it is available on GitHub[5].

The abundance for each spectral line is determined by fitting the synthetic line profile to the observed profile using the code SYNTHVB [57]. A conjunction of the code SYNTHVB with the code BinMag [58] enables the implementation of pre-computed departure coefficients, which represent the ratio of NLTE to LTE atomic level populations. The NLTE calculations are performed with a modified version of the DETAIL code [59], where the opacity package was updated as described by Mashonkina et al. [41]. We adopted the Ba II model atom of Mashonkina and Belyaev [60], and the Eu II model atom of Mashonkina and Gehren [61], which was updated by including data on inelastic collisions with hydrogen atoms from Storm et al. [62]. Classical 1D model atmospheres from the MARCS model grid [63], interpolated for given $T_{\rm eff}$, log g, and [Fe/H] of the stars, were used.

The method of the Ba isotope ratio determination relies on the fact that the odd isotopes are subject to HFS of the energy levels, and a higher $F_{\rm odd}$ results in a broader line profile and greater total absorbed energy. HFS primarily affects the ground state, meaning that the Ba II resonance lines can serve as a diagnostic of the Ba isotope ratio. In contrast, subordinate lines are almost unaffected by the adopted isotope ratio and can be used as

reliable indicators of barium abundance. This feature can be used for an F_{odd} determination by comparing abundances from the subordinate lines and the resonance lines computed with different F_{odd}. This idea was first proposed by Cowley and Frey [64], who pointed out the importance of taking HFS into account when determining Ba abundances. The abundance comparison method of the F_{odd} determination was applied to MP stars in the Milky Way [60,65–68] and in the Sculptor dwarf spheroidal galaxy [69], as well as to CEMP-s and CEMP-rs stars [30].

We analyzed four lines of Ba II: the strong resonance line at λ = 4934 Å, and the subordinate lines at λ = 5853 Å, 6141 Å, and 6496 Å. The resonance Ba II 4554 Å line is not covered by the available spectra of our sample stars. In our spectral synthesis calculations, we considered five Ba isotopes: ^{134}Ba, ^{135}Ba, ^{136}Ba, ^{137}Ba, and ^{138}Ba. We determined the Ba abundances from the resonance line using different F_{odd}: 0.10 (pure s-process), 0.18 (solar), 0.43, 0.62, 0.75 (pure r-process), and 1. Higher F_{odd} results in a stronger line and a lower derived barium abundance (Figure A2). When using F_{odd} = 0.1, we found 0.24 dex, 0.29 dex, and 0.34 dex higher abundances in BPS CS 29512-073, SDSS J1349-0229, and SDSS J1036+1212, respectively, compared to those derived with F_{odd} = 0.75 (Figure 1). The abundances from individual lines of Ba II are presented in Table 4.

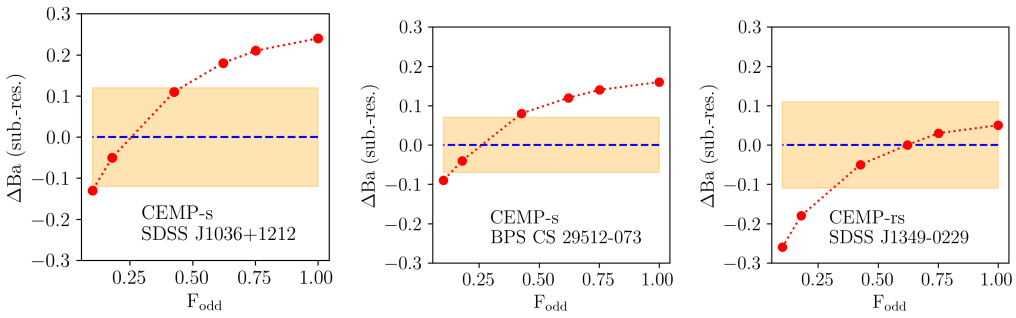

Figure 1. NLTE abundance difference between the subordinate and the resonance lines of Ba II as a function of F_{odd} in the sample stars (circles). Shaded area indicates the uncertainty in ΔBa(sub.-res.).

The impact of F_{odd} on the Ba II 4934 Å line profile might be less prominent compared to its impact on a total absorbed energy. In SDSS J1349-0229 and SDSS J1036+1212, EWs of the Ba II 4934 Å lines amount to 106 mÅ and 66 mÅ, respectively, while their best-fit spectra derived with different F_{odd} are almost indistinguishable (Figure A3). In the CEMP-s star BPS CS 29512-073 with a stronger Ba II 4934 Å line with EW = 150 mÅ, the s-process Ba isotope mixture provides a better fit compared to those computed with the r-process mixture (Figure A3).

We estimated an impact of 3D effects on the F_{odd} determination using the differences between 3D NLTE and 1D NLTE abundance corrections (Δ_{31}) for the Ba II lines available at the ChETEC-INFRA project webpage[6]. For a model atmosphere with T_{eff}/log g/[Fe/H]/[Ba/Fe] = 5900 K/4/−2/1, the differences Δ_{31} amount to −0.07, −0.02, −0.05, and −0.05 dex for the Ba II 4934 Å, 5853 Å, 6141 Å, and 6496 Å, respectively. The lower abundance from the resonance line compared to those from the subordinate lines results in a smaller F_{odd}. The corresponding shift of 0.03 dex in ΔBa(sub-res) results in the shifts in F_{odd} of −0.11, −0.04, and −0.03 in SDSS J1349-0229, BPS CS 29512-073, and SDSS J1036+1212, respectively, which can be considered minor compared to the uncertainties in F_{odd} determinations.

Table 4. NLTE and LTE abundances and EWs (mÅ) of the Ba II lines in the sample stars.

Name	**Ba II:**	**4934**						**5853**	**6141**	**6496**
		F_{odd}: **1.0**	**0.75**	**0.62**	**0.43**	**0.18**	**0.10**			
SDSS J1349-0229	NLTE	0.98	1.00	1.03	1.08	1.21	1.29	1.09	0.97	1.02
SDSS J1349-0229	LTE	1.08	1.10	1.13	1.18	1.31	1.39	1.11	1.18	1.22
SDSS J1349-0229	EW	106.2	106.2	106.2	106.2	106.2	106.2	24.2	66.6	57.2
BPS CS 29512-073	NLTE	1.24	1.25	1.27	1.32	1.43	1.49	1.40	1.23 [1]	1.39
BPS CS 29512-073	LTE	1.31	1.32	1.34	1.39	1.50	1.56	1.58	1.59 [1]	1.77
BPS CS 29512-073	EW	150.2	150.2	150.2	150.2	150.2	150.2	63.8	105.6	107.1
SDSS J1036+1212	NLTE	−0.36	−0.33	−0.30	−0.23	−0.07	0.01	–	−0.19	−0.05
SDSS J1036+1212	LTE	−0.38	−0.35	−0.32	−0.25	−0.09	−0.01	–	−0.26	−0.10
SDSS J1036+1212	EW	66.3	66.3	66.3	66.3	66.3	66.3	–	28.8	28.3

Note. [1]—the Ba II 6141 Å in BPS CS 29512-073 was excluded from the abundance analysis due to a significant contribution from the Fe I 6141 Å blending line, see Figure A4.

We determined the Eu abundance in BPS CS 29512-073 from the Eu II 3819 Å, 4129 Å, and 4205 Å lines, which yielded in NLTE $\log \varepsilon = -0.92$, -0.77, and -0.87, respectively. Our best-fit synthetic spectra together with the observed spectrum are presented in Figure A5. In the spectra of the two other stars, the lines of Eu II were not detected, and we estimated upper limits on their Eu abundances.

For each sample star, we provide the average NLTE abundance ratios in Table 5. We calculated the uncertainties in the abundance ratios and F_{odd} including the uncertainties in the stellar atmosphere parameters, continuum placement, as well as the dispersion of the individual line measurements; see Sitnova et al. [30] for details.

Table 5. NLTE abundance ratios and fractions of odd Ba isotopes in the sample stars.

Name	**[Ba/H]**		**[Eu/H]**		**[Ba/Eu]**	**[Ba/Fe]**		**[Eu/Fe]**	F_{odd}
SDSS J1349-0229	−1.14 (0.12)	<	−1.99 (0.22)	>	0.85 (0.23)	1.70 (0.15)	<	0.85 (0.15)	$0.65^{+0.35}_{-0.34}$
BPS CS 29512-073	−0.78 (0.09)		−1.36 (0.09)		0.59 (0.09)	1.10 (0.08)		0.52 (0.08)	$0.23^{+0.19}_{-0.10}$
SDSS J1036+1212	−2.28 (0.13)	<	−2.14 (0.22)	>	−0.15 (0.23)	0.98 (0.16)	<	1.13 (0.16)	$0.23^{+0.22}_{-0.11}$

Note. The solar abundances are taken from Lodders [70]. The total uncertainties are given in parentheses.

4. Results

A CEMP-rs star SDSS J1349-0229 shows $F_{odd} = 0.65^{+0.35}_{-0.34}$. Although the uncertainties are large, the possibility of a pure s-process or solar Ba isotope mixture can be excluded, while the derived F_{odd} agrees within the error bars with the i-process model predictions [32]. The derived F_{odd} aligns well with F_{odd} from 0.44 to 0.57 found in the CEMP-rs stars studied in Sitnova et al. [30].

In the CEMP-s stars, we found $F_{odd} = 0.23^{+0.19}_{-0.10}$ in BPS CS 29512-073 and $0.23^{+0.22}_{-0.11}$ in SDSS J1036+1212, which are consistent within the error bars with the solar value $F_{odd} = 0.18$ [10] and the F_{odd} values found in the CEMP-s stars studied in Sitnova et al. [30]. The derived F_{odd} values argue that a contribution from other n-capture sources besides the s-process to the chemical composition of the CEMP-s sample stars cannot be excluded. For example, in the solar system matter a contribution of 12% is attributed to the r-process [10]. Therefore, a similar r-process contribution can be expected for our CEMP-s sample stars.

Figure 2 shows F_{odd} as a function of [Ba/Eu] in the sample stars and our comparison sample from Sitnova et al. [30]. We also plotted a curve that represents a mixture of the s-process and the r-process material. For illustration, we applied a pure s-process ratio of [Ba/Eu] = 1.25 as computed for the solar system material by Prantzos et al. [10]. It is worth noting that individual models of AGB stars predict various [Ba/Eu] ratios. For example,

Lugaro et al. [71] found [Ba/Eu] from 0.57 to 1.09 for AGB stars with [Fe/H] = −2.3 and different masses.

Mixing s- and r-process material in equal proportions yields [Ba/Eu] = −0.6 and F_{odd} = 0.4. This demonstrates that the chemical composition of the CEMP stars with $F_{odd} \simeq 0.6$ and [Ba/Eu] > 0 cannot be explained by a mixture of s- and r-process material and those stars are i-process tracers. In contrast, there is at least one star in our comparison sample stars that possibly gained its n-capture element overabundances from a mixture of the s- and r-process material in compatible proportions, resulting in [Ba/Eu] = −0.29 and $F_{odd} = 0.38^{+0.53}_{-0.22}$. This star is 2MASS J09124370+0216236 and it could be considered a CEMP-r+s star (marked as a red open triangle in Figure 2).

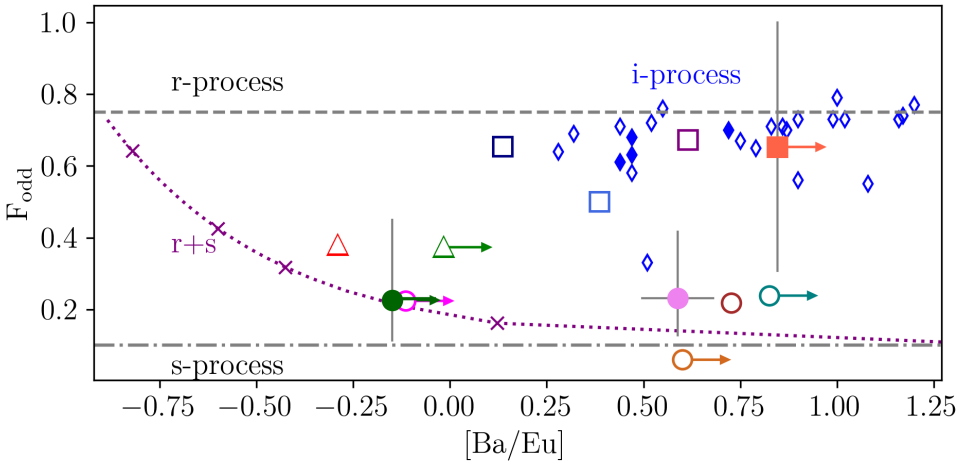

Figure 2. F_{odd} as a function of [Ba/Eu] in the sample stars: SDSS J1036+1212 (green circle), BPS CS 29512-073 (rosy circle), and SDSS J1349-0229 (orange square). The stars from Sitnova et al. [30] are shown with open symbols. For comparison, we show the theoretical predictions for the r-process (dashed line) and the s-process (dash-dotted line). The s- and r-process material mixture is shown with the dotted line, where crosses mark relative r- to s-process material contributions of 5, 1, and 0.1 (from left to right). The i-process predictions are shown with diamonds, where the filled diamonds correspond to the i-process models with [Fe/H] and [Ba/Fe] that fall in the parameter range of our sample stars.

5. Conclusions

We performed the NLTE abundance analysis of the Ba II lines in three CEMP stars and determined their F_{odd}. Our findings support the earlier classification of BPS CS 29512-073 and SDSS J1036+1212 as CEMP-s stars [33–35] and of SDSS J1349-0229 as a CEMP-rs star [33,35].

Our results are consistent with the finding of Sitnova et al. [30] about distinct F_{odd} in CEMP-s and CEMP-rs stars. In total, we have determined F_{odd} in 12 CEMP stars, and based on their [Ba/Eu] and F_{odd}, we grouped them as follows:

- CEMP-s stars with [Ba/Eu] > −0.1 and $F_{odd} < 0.25$. Heavy element abundances of these stars originate mainly from the s-process; however, a minor contribution from the r-process of less than 20% may still be present.
- CEMP-r + s stars with [Ba/Eu] < 0 and $F_{odd} > 0.3$. In these stars, their observed [Ba/Eu] and F_{odd} can be explained by a mixture of material produced by the r- and s-processes in compatible proportions of 1:2.
- CEMP-rs stars with [Ba/Eu] > 0 and $F_{odd} \simeq 0.6$. Heavy element abundances of these stars cannot be explained by a mixture of the material produced by the r- and s-processes, and they are the i-process tracers.

Among the 12 CEMP stars analyzed in this study and Sitnova et al. [30], four stars are identified as i-process tracers. For obtaining observational constraints on i-process nucleosynthesis, further NLTE abundance determinations for many chemical elements are required.

Author Contributions: Both authors contributed to conceptualization, methodology, validation, and writing. All authors have read and agreed to the published version of the manuscript.

Funding: This research received no external funding.

Data Availability Statement: The data are available in tables and figures, as well as open sources listed in text.

Acknowledgments: The authors thank the referees for providing valuable feedback.

Conflicts of Interest: The authors declare no conflict of interest.

Appendix A

Table A1. NLTE and LTE abundances from the Fe I and Fe II lines in the sample stars together with their atomic data and EWs.

Species	λ, Å	E_{exc}, eV	log gf	log ε NLTE	log ε LTE	EW, mÅ	log ε NLTE	log ε LTE	EW, mÅ	log ε NLTE	log ε LTE	EW, mÅ
	Å	eV		BPS CS 29512-073			SDSS J1036+1212			SDSS J1349-0229		
Fe I	4891.49	2.85	−0.11	5.57	5.55	82.5	4.44	4.27	23.9	4.71	4.61	24.6
Fe I	4903.31	2.88	−0.93	5.51	5.47	36.5						
Fe I	4918.99	2.87	−0.34	5.51	5.48	66.9						
Fe I	4938.81	2.88	−1.08	5.46	5.42	27.7						
Fe I	4966.09	3.33	−0.89	5.55	5.51	21.1						
Fe I	5001.86	3.88	0.01	5.39	5.34	29.1						
Fe I	5049.82	2.28	−1.36	5.57	5.53	46.7						
Fe I	5068.77	2.94	−1.04	5.54	5.50	30.6						
Fe I	5074.75	4.22	−0.20	5.71	5.66	20.6						
Fe I	5171.60	1.48	−1.75	5.58	5.54	64.8				4.83	4.75	16.9
Fe I	5191.45	3.04	−0.55	5.49	5.45	47.8						
Fe I	5192.34	3.00	−0.52	5.55	5.51	54.1						
Fe I	5194.94	1.56	−2.09	5.57	5.53	46.6						
Fe I	5215.18	3.27	−0.93	5.50	5.46	20.7						
Fe I	5216.27	1.61	−2.10	5.54	5.50	42.6						
Fe I	5217.39	3.21	−1.07	5.44	5.41	16.3						
Fe I	5232.94	2.94	−0.07	5.44	5.42	74.9	4.22	4.04	15.3	4.67	4.57	22.1
Fe I	5266.55	3.00	−0.39	5.45	5.41	55.5						
Fe I	5281.79	3.04	−0.83	5.49	5.45	34.0						
Fe I	5283.62	3.24	−0.52	5.54	5.49	41.3						
Fe I	5302.30	3.28	−0.88	5.59	5.55	25.9						
Fe I	5307.36	1.61	−2.99	5.59	5.55	11.2						
Fe I	5324.18	3.21	−0.10	5.45	5.41	60.1						
Fe I	5339.93	3.27	−0.68	5.51	5.47	31.7						
Fe I	5367.47	4.42	0.55	5.34	5.28	28.1						
Fe I	5369.96	4.37	0.54	5.40	5.34	32.4						
Fe I	5383.37	4.31	0.50	5.54	5.48	39.6						
Fe I	5393.17	3.24	−0.71	5.46	5.42	29.3						
Fe I	5400.50	4.37	−0.15	5.54	5.49	12.8						
Fe I	5415.20	4.39	0.51	5.51	5.45	35.4						
Fe I	5424.07	4.32	0.52	5.57	5.51	42.1						
Fe I	5569.62	3.42	−0.54	5.51	5.46	31.5						
Fe I	5572.84	3.40	−0.31	5.46	5.41	41.0						
Fe I	5576.09	3.43	−1.00	5.67	5.63	19.3						
Fe I	5586.76	3.37	−0.14	5.47	5.42	51.5						
Fe I	5615.64	3.33	0.05	5.43	5.39	61.9						

Table A1. *Cont.*

Species	λ, Å	E_{exc}, eV	log gf	log ε NLTE	log ε LTE	EW, mÅ	log ε NLTE	log ε LTE	EW, mÅ	log ε NLTE	log ε LTE	EW, mÅ
	Å	eV		BPS CS 29512-073			SDSS J1036+1212			SDSS J1349-0229		
Fe I	6024.06	4.55	−0.11	5.69	5.65	14.1						
Fe I	6136.61	2.45	−1.50	5.62	5.58	37.3						
Fe I	6137.69	2.59	−1.37	5.53	5.49	32.9						
Fe I	6191.56	2.43	−1.42	5.48	5.44	35.3						
Fe I	6230.72	2.56	−1.28	5.56	5.52	40.1						
Fe I	6252.55	2.40	−1.76	5.63	5.59	28.2						
Fe I	6301.50	3.65	−0.72	5.53	5.48	17.1						
Fe I	6335.33	2.20	−2.23	5.58	5.54	16.9						
Fe I	6393.60	2.43	−1.43	5.42	5.38	32.9						
Fe I	6400.00	3.60	−0.52	5.65	5.60	32.0						
Fe I	6421.35	2.28	−2.01	5.59	5.55	22.0						
Fe I	6430.84	2.18	−1.95	5.57	5.53	28.0						
Fe I	6494.98	2.40	−1.27	5.57	5.53	48.9						
Fe II	4491.40	2.86	−2.65	5.57	5.57	23.7						
Fe II	4508.28	2.86	−2.23	5.55	5.55	40.9						
Fe II	4923.92	2.89	−1.39	5.62	5.62	79.8	4.30	4.30	26.6			
Fe II	5018.44	2.89	−1.23	5.62	5.62	87.7	4.17	4.17	28.4	4.51	4.51	27.1
Fe II	5169.03	2.89	−1.14				4.06	4.06	27.6	4.70	4.70	39.5
Fe II	5197.57	3.23	−2.24	5.57	5.57	27.0						
Fe II	5234.62	3.22	−2.17	5.55	5.55	29.5						
Fe II	5276.00	3.20	−2.10	5.51	5.51	31.9						
Fe II	6456.38	3.90	−2.07	5.58	5.58	12.6						

Table A2. The HFS and isotopic components of the Ba II lines. Solar isotope mixture is adopted.

A	λ, Å	E_{exc}, eV	log gf	A	λ, Å	E_{exc}, eV	log gf
137	4553.9980	0.0000	−1.586	137	6141.7086	0.7036	−2.254
137	4553.9991	0.0000	−1.586	137	6141.7086	0.7036	−1.446
137	4553.9993	0.0000	−1.984	137	6141.7094	0.7036	−3.400
135	4554.0009	0.0000	−1.817	135	6141.7105	0.7036	−1.677
135	4554.0021	0.0000	−1.817	135	6141.7107	0.7036	−2.485
135	4554.0025	0.0000	−2.215	135	6141.7113	0.7036	−3.631
130	4554.0310	0.0000	−2.805	138	6141.7129	0.7036	−0.214
132	4554.0315	0.0000	−2.826	136	6141.7140	0.7036	−1.175
134	4554.0319	0.0000	−1.447	137	6141.7146	0.7036	−1.652
136	4554.0323	0.0000	−0.935	137	6141.7154	0.7036	−2.157
138	4554.0336	0.0000	0.026	134	6141.7154	0.7036	−1.687
135	4554.0479	0.0000	−1.370	135	6141.7157	0.7036	−1.883
137	4554.0503	0.0000	−1.139	137	6141.7163	0.7036	−3.224
135	4554.0506	0.0000	−1.817	135	6141.7163	0.7036	−2.388
135	4554.0518	0.0000	−2.516	132	6141.7169	0.7036	−3.066
137	4554.0536	0.0000	−1.586	135	6141.7170	0.7036	−3.455
137	4554.0547	0.0000	−2.285	137	6141.7174	0.7036	−1.902
137	4934.0298	0.0000	−1.627	130	6141.7183	0.7036	−3.045
135	4934.0339	0.0000	−1.858	137	6141.7183	0.7036	−2.270
137	4934.0419	0.0000	−2.326	135	6141.7184	0.7036	−2.133
135	4934.0447	0.0000	−2.557	137	6141.7188	0.7036	−2.224
130	4934.0744	0.0000	−3.147	135	6141.7191	0.7036	−2.501
132	4934.0750	0.0000	−3.168	135	6141.7198	0.7036	−2.455
134	4934.0755	0.0000	−1.789	137	6496.8826	0.6043	−2.821
136	4934.0758	0.0000	−1.277	135	6496.8857	0.6043	−3.052
138	4934.0773	0.0000	−0.316	137	6496.8873	0.6043	−2.122
135	4934.0922	0.0000	−1.858	135	6496.8901	0.6043	−2.353
137	4934.0950	0.0000	−1.627	137	6496.8959	0.6043	−1.675
135	4934.1030	0.0000	−1.858	135	6496.8977	0.6043	−1.906

Table A2. *Cont.*

A	λ, Å	E_{exc}, eV	log gf	A	λ, Å	E_{exc}, eV	log gf
137	4934.1071	0.0000	−1.627	138	6496.8977	0.6043	−0.510
137	5853.6685	0.6043	−3.031	136	6496.8988	0.6043	−1.471
137	5853.6701	0.6043	−2.973	134	6496.9004	0.6043	−1.983
137	5853.6703	0.6043	−3.177	137	6496.9015	0.6043	−2.520
135	5853.6705	0.6043	−3.262	132	6496.9021	0.6043	−3.362
135	5853.6715	0.6043	−3.204	135	6496.9025	0.6043	−2.751
135	5853.6718	0.6043	−3.408	137	6496.9035	0.6043	−2.122
137	5853.6720	0.6043	−3.575	130	6496.9037	0.6043	−3.341
137	5853.6723	0.6043	−3.177	135	6496.9044	0.6043	−2.353
135	5853.6734	0.6043	−3.806	137	6496.9082	0.6043	−2.122
137	5853.6739	0.6043	−2.876	135	6496.9088	0.6043	−2.353
135	5853.6740	0.6043	−3.408				
138	5853.6742	0.6043	−1.167				
135	5853.6750	0.6043	−3.107				
136	5853.6751	0.6043	−2.128				
137	5853.6755	0.6043	−2.429				
137	5853.6758	0.6043	−2.973				
134	5853.6764	0.6043	−2.640				
135	5853.6766	0.6043	−2.660				
135	5853.6769	0.6043	−3.204				
137	5853.6809	0.6043	−3.031				
135	5853.6812	0.6043	−3.262				

Note. We provide a tool for generating the lists of Ba II lines for a given F_{odd}, which is available on https://github.com/sitamih/ba_linelist (accessed on 28 April 2026).

Table A3. The HFS and isotopic components of the Eu II lines. Solar isotope mixture is adopted.

A	λ, Å	E_{exc}, eV	log gf	A	λ, Å	E_{exc}, eV	log gf	A	λ, Å	E_{exc}, eV	log gf
151	3819.57682	0.00	−0.940	151	4129.59676	0.00	−1.832	151	4204.89432	0.00	−1.432
151	3819.59380	0.00	−0.831	151	4129.60032	0.00	−1.355	151	4204.89746	0.00	−1.733
151	3819.59557	0.00	−1.609	151	4129.61392	0.00	−1.636	151	4204.90262	0.00	−2.687
151	3819.61750	0.00	−0.722	151	4129.61868	0.00	−1.297	151	4204.92018	0.00	−1.256
151	3819.62005	0.00	−1.419	151	4129.62223	0.00	−1.832	151	4204.92534	0.00	−1.550
151	3819.62182	0.00	−2.827	151	4129.63885	0.00	−1.577	151	4204.93242	0.00	−2.578
153	3819.64347	0.00	−0.902	151	4129.64460	0.00	−1.167	151	4204.95715	0.00	−1.093
151	3819.64771	0.00	−0.617	151	4129.64936	0.00	−1.636	151	4204.96423	0.00	−1.491
151	3819.65124	0.00	−1.365	151	4129.67183	0.00	−1.614	151	4204.97307	0.00	−2.687
153	3819.65180	0.00	−1.571	153	4129.67754	0.00	−1.794	153	4204.99375	0.00	−1.394
153	3819.65248	0.00	−0.793	151	4129.67829	0.00	−1.016	153	4204.99554	0.00	−1.695
151	3819.65379	0.00	−2.681	153	4129.68030	0.00	−1.317	153	4204.99834	0.00	−2.649
153	3819.66347	0.00	−2.789	153	4129.68396	0.00	−1.598	151	4205.00512	0.00	−0.947
153	3819.66415	0.00	−1.381	151	4129.68404	0.00	−1.577	153	4205.00564	0.00	−1.218
153	3819.66433	0.00	−0.684	153	4129.68728	0.00	−1.259	153	4205.00844	0.00	−1.512
153	3819.67847	0.00	−0.579	153	4129.69004	0.00	−1.794	153	4205.01198	0.00	−2.540
153	3819.67915	0.00	−2.643	153	4129.69428	0.00	−1.539	151	4205.01397	0.00	−1.525
153	3819.67932	0.00	−1.327	153	4129.69760	0.00	−1.129	153	4205.02258	0.00	−1.055
151	3819.68419	0.00	−0.518	153	4129.70092	0.00	−1.598	151	4205.02439	0.00	−3.030
151	3819.68895	0.00	−1.407	153	4129.70920	0.00	−1.576	153	4205.02612	0.00	−1.453
151	3819.69249	0.00	−2.768	153	4129.71182	0.00	−0.978	153	4205.03002	0.00	−2.649
153	3819.69428	0.00	−0.480	151	4129.71321	0.00	−1.800	153	4205.04430	0.00	−0.909
153	3819.69680	0.00	−1.369	153	4129.71513	0.00	−1.539	153	4205.04820	0.00	−1.487
153	3819.69765	0.00	−2.730	151	4129.72004	0.00	−0.865	153	4205.05198	0.00	−2.992
153	3819.71099	0.00	−0.387	151	4129.72650	0.00	−1.614	151	4205.06395	0.00	−0.816

Table A3. *Cont.*

A	λ, Å	E_{exc}, eV	log gf	A	λ, Å	E_{exc}, eV	log gf	A	λ, Å	E_{exc}, eV	log gf
153	3819.71594	0.00	−1.559	153	4129.72958	0.00	−1.762	153	4205.07042	0.00	−0.778
153	3819.71846	0.00	−3.058	153	4129.73063	0.00	−0.827	153	4205.07419	0.00	−1.670
151	3819.72663	0.00	−0.425	153	4129.73324	0.00	−1.576	151	4205.07437	0.00	−1.708
151	3819.73292	0.00	−1.597	153	4129.75490	0.00	−0.683	153	4205.10044	0.00	−0.658
151	3819.73769	0.00	−3.096	153	4129.75594	0.00	−1.762	151	4205.13344	0.00	−0.696
				151	4129.77018	0.00	−0.721				
				151	4129.77701	0.00	−1.800				

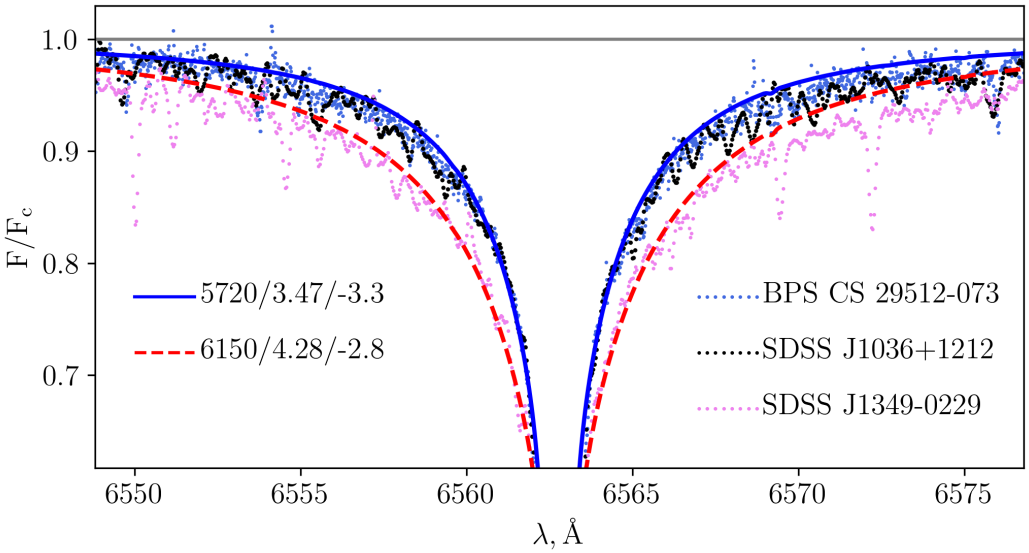

Figure A1. The Hα line profiles in the observed spectra (circles) of the sample stars along with the synthetic LTE spectra (lines). See legend for designations.

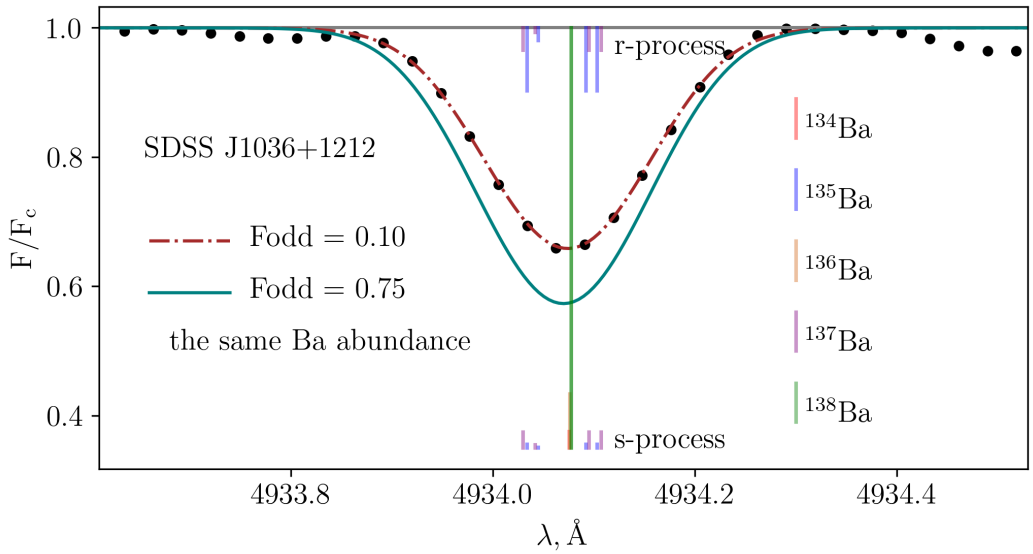

Figure A2. The Ba II 4934 Å line profiles in the observed spectrum of SDSS J1036+1212 (circles) along with the synthetic NLTE spectra computed with the same Ba abundance but different F_{odd} = 0.10 and 0.75. Vertical dashes show the relative contribution of different Ba isotopes to the r-process and s-process; see legend for isotopes designations.

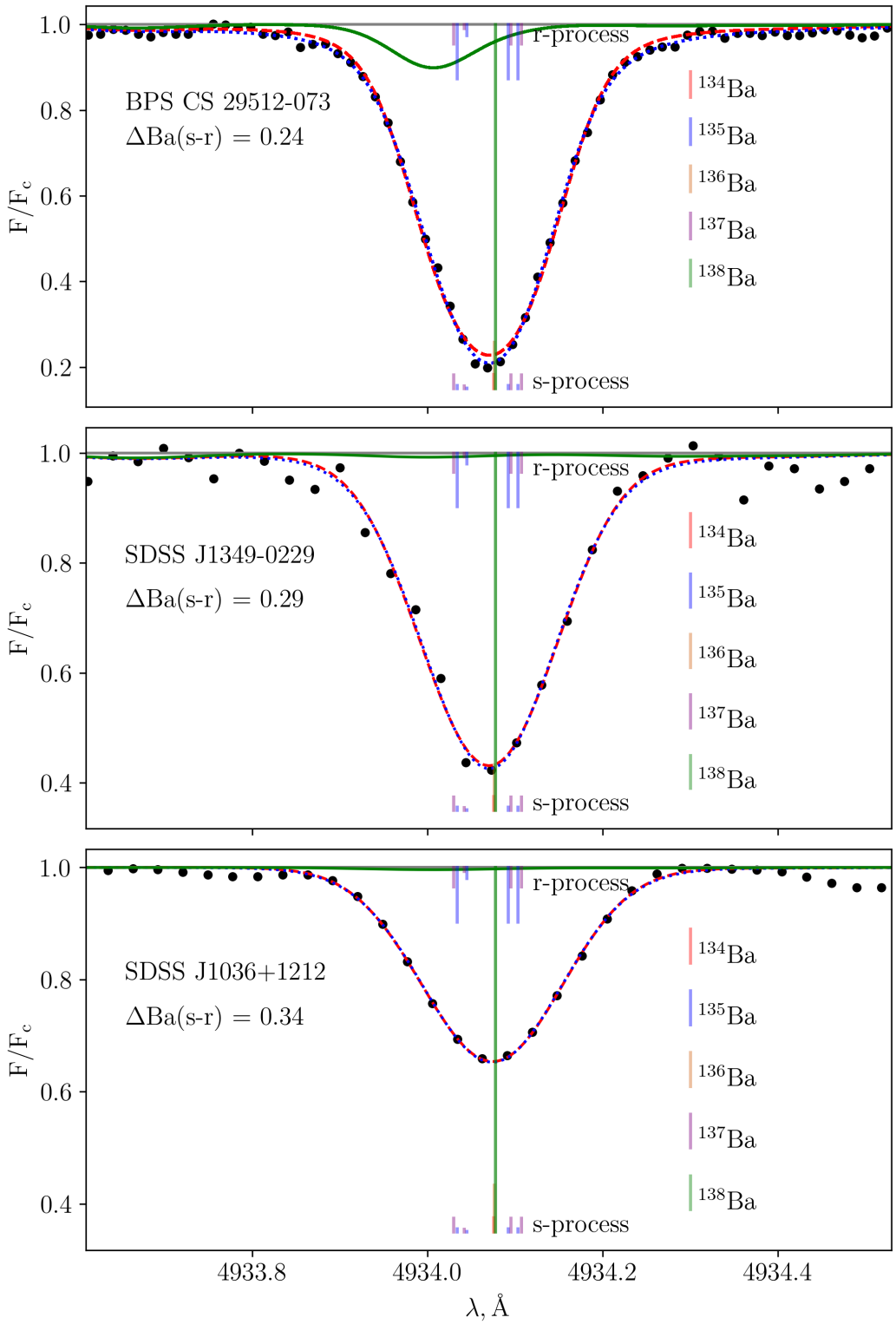

Figure A3. Ba II 4934 Å line profiles in the observed spectra (circles) of the sample stars along with the synthetic best-fit NLTE spectra, derived using pure r-process (dashed red line) and pure s-process (dotted blue line) Ba isotope mixtures. In the CEMP-s star BPS CS 29512-073, the s-process Ba isotope mixture provides a better fit compared to those computed with the r-process mixture. In SDSS J1349-0229 and SDSS J1036+1212, the Ba II 4934 Å lines are weaker compared to those in BPS CS 29512-073 and their best-fit spectra derived with the s- and r-process Ba isotope mixtures are almost indistinguishable. For each star, the abundance difference between the best-fit spectra derived with the s- and r-process Ba isotope mixtures (ΔBa(s-r)) are indicated. Solid green line shows a spectrum, calculated neglecting the Ba II 4934 Å line; the blending lines are attributed to the Fe I 4934.01 Å and the CH 4933.70 Å lines. Vertical dashes show the relative contribution of different Ba isotopes to the r-process and s-process; see legend for isotopes designations.

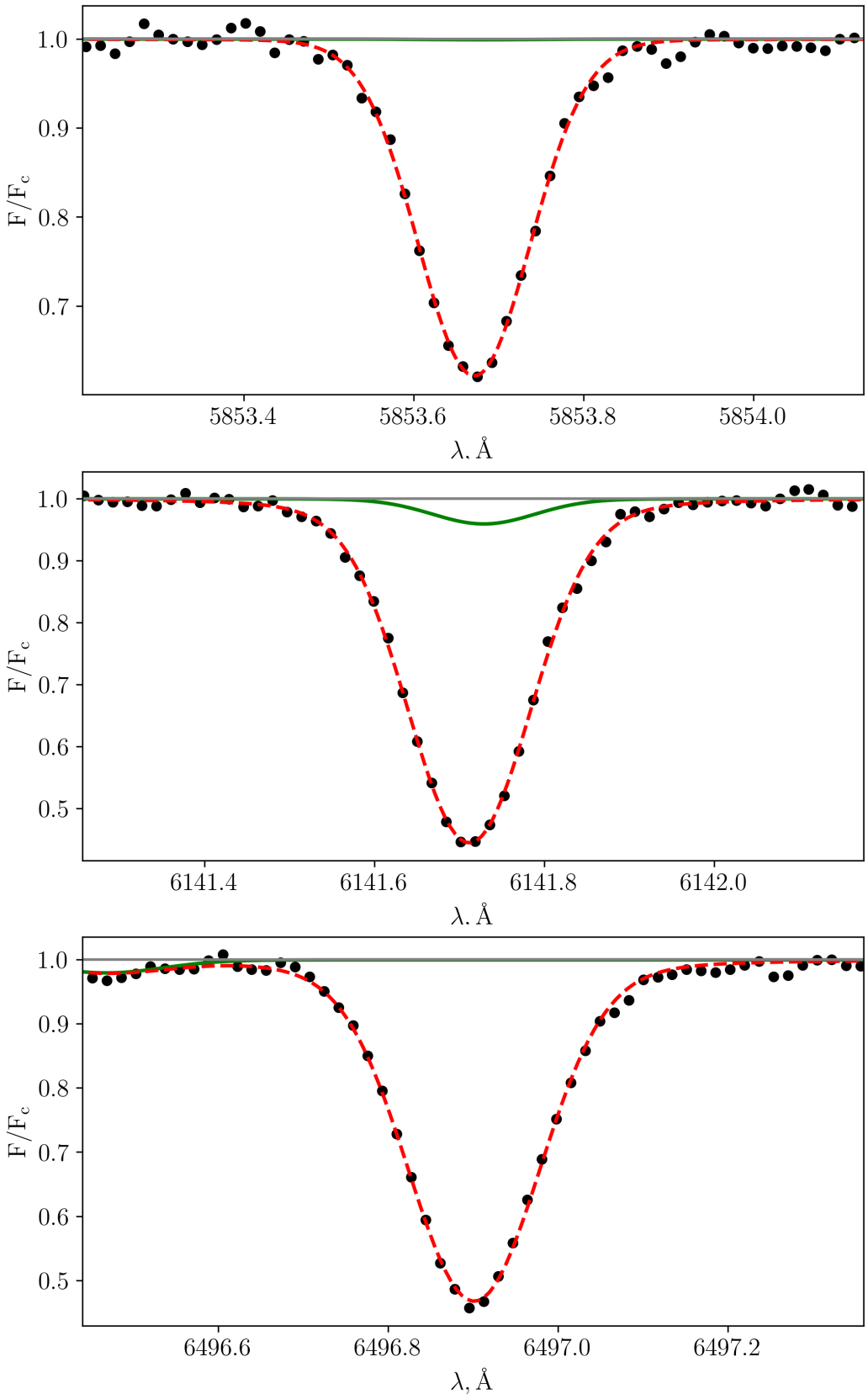

Figure A4. Ba II line profiles in the observed spectra (circles) of the BPS CS 29512-073 stars along with the synthetic best-fit NLTE spectra (dashed line). Solid green line shows a spectrum, calculated neglecting the Ba II lines; the blending line is attributed to the Fe I 6141.73 Å line (middle panel).

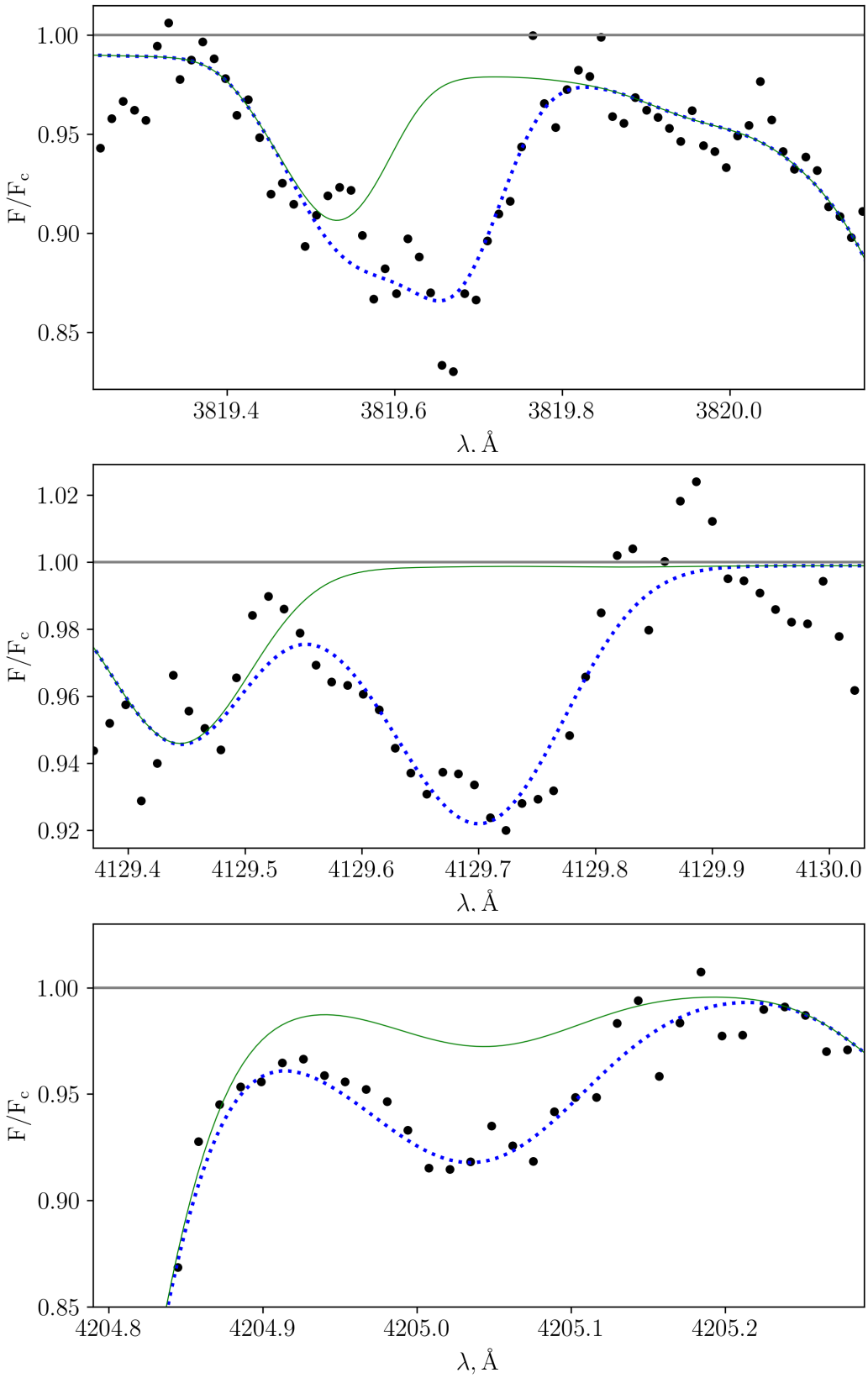

Figure A5. Eu II line profiles in the observed spectra (circles) of the BPS CS 29512-073 stars along with the synthetic best-fit NLTE spectra (dotted line). Solid green line shows a spectrum, calculated neglecting the Eu II lines; the blending lines are attributed to the Fe I 3819.49 Å Cr I 3819.56 Å (**top** panel), Fe I 4129.26 Å (**middle** panel), CH 4204.70 Å, and the V II 4205.05 Å (**bottom** panel) lines.

Notes

[1] We use a standard designation, $[X/Y] = \log(N_X/N_Y)_* - \log(N_X/N_Y)_\odot$, where N_X and N_Y are total number densities of elements X and Y, respectively.
[2] http://archive.eso.org/wdb/wdb/adp/phase3_main/form (accessed on 28 April 2026).
[3] https://spectrum.inasan.ru/nLTE2/ (accessed on 28 April 2026).
[4] We use a standard abundance designation, $\log \varepsilon(X) = \log(N_X/N_H) + 12$, where N_X and N_H are total number densities of element X and hydrogen, respectively.
[5] https://github.com/sitamih/ba_linelist (accessed on 28 April 2026).
[6] https://www.chetec-infra.eu/3dnlte/abundance-corrections/barium/ (accessed on 28 April 2026).

References

1. Burbidge , E.M.; Burbidge, G.R.; Fowler, W.A.; Hoyle, F. Synthesis of the Elements in Stars. *Rev. Mod. Phys.* **1957**, *29*, 547–650. [CrossRef]
2. Cowan, J.J.; Rose, W.K. Production of ^{14}C and neutrons in red giants. *Astrophys. J.* **1977**, *212*, 149–158. [CrossRef]
3. Gallino, R.; Arlandini, C.; Busso, M.; Lugaro, M.; Travaglio, C.; Straniero, O.; Chieffi, A.; Limongi, M. Evolution and Nucleosynthesis in Low-Mass Asymptotic Giant Branch Stars. II. Neutron Capture and the S-Process. *Astrophys. J.* **1998**, *497*, 388–403. [CrossRef]
4. Herwig, F. Evolution of Asymptotic Giant Branch Stars. *Annu. Rev. Astron. Astrophys.* **2005**, *43*, 435–479. [CrossRef]
5. Herwig, F.; Pignatari, M.; Woodward, P.R.; Porter, D.H.; Rockefeller, G.; Fryer, C.L.; Bennett, M.; Hirschi, R. Convective-reactive Proton-^{12}C Combustion in Sakurai's Object (V4334 Sagittarii) and Implications for the Evolution and Yields from the First Generations of Stars. *Astrophys. J.* **2011**, *727*, 89. [CrossRef]
6. Cristallo, S.; Karinkuzhi, D.; Goswami, A.; Piersanti, L.; Gobrecht, D. Constraints of the Physics of Low-mass AGB Stars from CH and CEMP Stars. *Astrophys. J.* **2016**, *833*, 181. [CrossRef]
7. Choplin, A.; Siess, L.; Goriely, S. The intermediate neutron capture process. III. The i-process in AGB stars of different masses and metallicities without overshoot. *Astron. Astrophys.* **2022**, *667*, A155. [CrossRef]
8. Choplin, A.; Siess, L.; Goriely, S.; Martinet, S. The intermediate neutron capture process. V. The i-process in AGB stars with overshoot. *Astron. Astrophys.* **2024**, *684*, A206. [CrossRef]
9. Denissenkov, P.A.; Herwig, F.; Woodward, P.; Andrassy, R.; Pignatari, M.; Jones, S. The i-process yields of rapidly accreting white dwarfs from multicycle He-shell flash stellar evolution models with mixing parametrizations from 3D hydrodynamics simulations. *Mon. Not. R. Astron. Soc.* **2019**, *488*, 4258–4270. [CrossRef]
10. Prantzos, N.; Abia, C.; Cristallo, S.; Limongi, M.; Chieffi, A. Chemical evolution with rotating massive star yields II. A new assessment of the solar s- and r-process components. *Mon. Not. R. Astron. Soc.* **2020**, *491*, 1832–1850. [CrossRef]
11. Preston, G.W.; Sneden, C. The Incidence of Binaries among Very Metal-poor Carbon Stars. *Astrophys. J.* **2001**, *122*, 1545–1560. [CrossRef]
12. Lucatello, S.; Tsangarides, S.; Beers, T.C.; Carretta, E.; Gratton, R.G.; Ryan, S.G. The Binary Frequency Among Carbon-enhanced, s-Process-rich, Metal-poor Stars. *Astrophys. J.* **2005**, *625*, 825–832. [CrossRef]
13. Starkenburg, E.; Shetrone, M.D.; McConnachie, A.W.; Venn, K.A. Binarity in carbon-enhanced metal-poor stars. *Mon. Not. R. Astron. Soc.* **2014**, *441*, 1217–1229. [CrossRef]
14. Beers, T.C.; Christlieb, N. The Discovery and Analysis of Very Metal-Poor Stars in the Galaxy. *Annu. Rev. Astron. Astrophys.* **2005**, *43*, 531–580. [CrossRef]
15. Jonsell, K.; Barklem, P.S.; Gustafsson, B.; Christlieb, N.; Hill, V.; Beers, T.C.; Holmberg, J. The Hamburg/ESO R-process enhanced star survey (HERES). III. HE 0338-3945 and the formation of the r + s stars. *Astron. Astrophys.* **2006**, *451*, 651–670. [CrossRef]
16. Abate, C.; Stancliffe, R.J.; Liu, Z.W. How plausible are the proposed formation scenarios of CEMP-r/s stars? *Astron. Astrophys.* **2016**, *587*, A50. [CrossRef]
17. Hansen, C.J.; Hansen, T.T.; Koch, A.; Beers, T.C.; Nordström, B.; Placco, V.M.; Andersen, J. Abundances and kinematics of carbon-enhanced metal-poor stars in the Galactic halo. A new classification scheme based on Sr and Ba. *Astron. Astrophys.* **2019**, *623*, A128. [CrossRef]
18. Karinkuzhi, D.; Van Eck, S.; Goriely, S.; Siess, L.; Jorissen, A.; Merle, T.; Escorza, A.; Masseron, T. Low-mass low-metallicity AGB stars as an efficient i-process site explaining CEMP-rs stars. *Astron. Astrophys.* **2021**, *645*, A61. [CrossRef]
19. Goswami, P.P.; Rathour, R.S.; Goswami, A. Spectroscopic study of CEMP-(s & r/s) stars. Revisiting classification criteria and formation scenarios, highlighting i-process nucleosynthesis. *Astron. Astrophys.* **2021**, *649*, A49. [CrossRef]
20. Zacs, L.; Nissen, P.E.; Schuster, W.J. The chemical composition of HD 196944: A carbon and s-process rich, very metal-poor star. *Astron. Astrophys.* **1998**, *337*, 216–222.
21. Van Eck, S.; Goriely, S.; Jorissen, A.; Plez, B. Discovery of three lead-rich stars. *Nature* **2001**, *412*, 793–795. [CrossRef] [PubMed]

22. Aoki, W.; Ryan, S.G.; Norris, J.E.; Beers, T.C.; Ando, H.; Tsangarides, S. A Subaru/High Dispersion Spectrograph Study of Lead (Pb) Abundances in Eight s-Process Element-rich, Metal-poor Stars. *Astrophys. J.* **2002**, *580*, 1149–1158. [CrossRef] [PubMed]
23. Jonsell, K.; Edvardsson, B.; Gustafsson, B.; Magain, P.; Nissen, P.E.; Asplund, M. Chemical abundances in 43 metal-poor stars. *Astron. Astrophys.* **2005**, *440*, 321–343. [CrossRef]
24. Masseron, T.; Johnson, J.A.; Plez, B.; van Eck, S.; Primas, F.; Goriely, S.; Jorissen, A. A holistic approach to carbon-enhanced metal-poor stars. *Astron. Astrophys.* **2010**, *509*, A93. [CrossRef]
25. Roederer, I.U.; Preston, G.W.; Thompson, I.B.; Shectman, S.A.; Sneden, C.; Burley, G.S.; Kelson, D.D. A Search for Stars of Very Low Metal Abundance. VI. Detailed Abundances of 313 Metal-poor Stars. *Astrophys. J.* **2014**, *147*, 136. [CrossRef]
26. Placco, V.M.; Beers, T.C.; Ivans, I.I.; Filler, D.; Imig, J.A.; Roederer, I.U.; Abate, C.; Hansen, T.; Cowan, J.J.; Frebel, A.; et al. Hubble Space Telescope Near-Ultraviolet Spectroscopy of Bright CEMP-s Stars. *Astrophys. J.* **2015**, *812*, 109. [CrossRef]
27. Mittal, S.; Roederer, I.U. New Stellar Parameters, Metallicities, and Elemental Abundance Ratios for 311 Metal-poor Stars. *Astrophys. J.* **2025**, *169*, 172. [CrossRef]
28. Roederer, I.U.; Placco, V.M.; Karakas, A.I.; Den Hartog, E.A.; Beers, T.C. Abundances of Rarely Detected s-process Elements Derived from the Ultraviolet Spectrum of the s-process-enhanced Metal-poor Star HD 196944. *Astrophys. J.* **2025**, *995*, 2. [CrossRef]
29. Abate, C.; Pols, O.R.; Izzard, R.G.; Karakas, A.I. Carbon-enhanced metal-poor stars: A window on AGB nucleosynthesis and binary evolution. II. Statistical analysis of a sample of 67 CEMP-s stars. *Astron. Astrophys.* **2015**, *581*, A22. [CrossRef]
30. Sitnova, T.M.; Mashonkina, L.I.; Romanovskaya, A.M.; Giribaldi, R.E.; Choplin, A. Distinct barium isotope ratios in CEMP-s and CEMP-rs stars. *Astron. Astrophys.* **2025**, *704*, A103. [CrossRef]
31. Van Eck, S.; Giribaldi, R.; Merle, T.; Lambotte, A.; Karinkuzhi, D.; Goriely, S.; Choplin, A.; Storm, N.; Gerber, J.; Siess, L.; et al. From the s-Process to the i-Process: A New Perspective on the Chemical Enrichment of Extrinsic Stars. *Galaxies* **2024**, *12*, 89. [CrossRef]
32. Choplin, A.; Goriely, S.; Siess, L.; Martinet, S. Synthesis of actinides and short-lived radionuclides during i-process nucleosynthesis in AGB stars. *Eur. Phys. J. A* **2025**, *61*, 68. [CrossRef]
33. Behara, N.T.; Bonifacio, P.; Ludwig, H.G.; Sbordone, L.; González Hernández, J.I.; Caffau, E. Three carbon-enhanced metal-poor dwarf stars from the SDSS. Chemical abundances from CO^{5}BOLD 3D hydrodynamical model atmospheres. *Astron. Astrophys.* **2010**, *513*, A72. [CrossRef]
34. Allen, D.M.; Ryan, S.G.; Rossi, S.; Beers, T.C.; Tsangarides, S.A. Elemental abundances and classification of carbon-enhanced metal-poor stars. *Astron. Astrophys.* **2012**, *548*, A34. [CrossRef]
35. Riyas, A.M.; Karinkuzhi, D.; Van Eck, S.; Choplin, A.; Goriely, S.; Siess, L.; Keerthy, M.V.; Jorissen, A.; Merle, T. Abundance of Heavy r-process Elements in CEMP-rs Stars: The Role of the i-process. *Astrophys. J.* **2026**, *997*, 44. [CrossRef]
36. Mucciarelli, A.; Bellazzini, M.; Massari, D. Exploiting the Gaia EDR3 photometry to derive stellar temperatures. *Astron. Astrophys.* **2021**, *653*, A90. [CrossRef]
37. Green, G.M.; Schlafly, E.; Zucker, C.; Speagle, J.S.; Finkbeiner, D. A 3D Dust Map Based on Gaia, Pan-STARRS 1, and 2MASS. *Astrophys. J.* **2019**, *887*, 93. [CrossRef]
38. Casagrande, L.; VandenBerg, D.A. On the use of Gaia magnitudes and new tables of bolometric corrections. *Mon. Not. R. Astron. Soc.* **2018**, *479*, L102–L107. [CrossRef]
39. Lindegren, L.; Bastian, U.; Biermann, M.; Bombrun, A.; de Torres, A.; Gerlach, E.; Geyer, R.; Hernández, J.; Hilger, T.; Hobbs, D.; et al. Gaia Early Data Release 3. Parallax bias versus magnitude, colour, and position. *Astron. Astrophys.* **2021**, *649*, A4. [CrossRef]
40. Bailer-Jones, C.A.L. Estimating Distances from Parallaxes. *Publ. Astron. Soc. Pac.* **2015**, *127*, 994. [CrossRef]
41. Mashonkina, L.; Gehren, T.; Shi, J.R.; Korn, A.J.; Grupp, F. A non-LTE study of neutral and singly-ionized iron line spectra in 1D models of the Sun and selected late-type stars. *Astron. Astrophys.* **2011**, *528*, A87. [CrossRef]
42. Mashonkina, L.; Pakhomov, Y.; Sitnova, T.; Smogorzhevskii, A.; Jablonka, P.; Hill, V. 1D non-LTE corrections for chemical abundance analyses of very metal-poor stars. *Mon. Not. R. Astron. Soc.* **2023**, *524*, 3526–3536. [CrossRef]
43. Mashonkina, L.; Sitnova, T.; Yakovleva, S.A.; Belyaev, A.K. Influence of inelastic collisions with hydrogen atoms on the non-local thermodynamic equilibrium line formation for Fe I and Fe II in the 1D model atmospheres of late-type stars. *Astron. Astrophys.* **2019**, *631*, A43. [CrossRef]
44. Sitnova, T.; Zhao, G.; Mashonkina, L.; Chen, Y.; Liu, F.; Pakhomov, Y.; Tan, K.; Bolte, M.; Alexeeva, S.; Grupp, F.; et al. Systematic Non-LTE Study of the $-2.6 <$ [Fe/H] < 0.2 F and G dwarfs in the Solar Neighborhood. I. Stellar Atmosphere Parameters. *Astrophys. J.* **2015**, *808*, 148. [CrossRef]
45. Casagrande, L.; Ramírez, I.; Meléndez, J.; Bessell, M.; Asplund, M. An absolutely calibrated T_{eff} scale from the infrared flux method. Dwarfs and subgiants. *Astron. Astrophys.* **2010**, *512*, A54. [CrossRef]
46. Frebel, A.; Casey, A.R.; Jacobson, H.R.; Yu, Q. Deriving Stellar Effective Temperatures of Metal-poor Stars with the Excitation Potential Method. *Astrophys. J.* **2013**, *769*, 57. [CrossRef]
47. Piskunov, N.E.; Kupka, F.; Ryabchikova, T.A.; Weiss, W.W.; Jeffery, C.S. VALD: The Vienna Atomic Line Data Base. *Astron. Astrophys. Suppl.* **1995**, *112*, 525.

48. Pakhomov, Y.V.; Ryabchikova, T.A.; Piskunov, N.E. Hyperfine Splitting in the VALD Database of Spectral-line Parameters. *Astron. Rep.* **2019**, *63*, 1010–1021. [CrossRef]
49. Miles, B.M.; Wiese, W.L. Critical Evaluation of Transition Probabilities for Ba I and Ba II. *At. Data Nucl. Data Tables* **1969**, *1*, 1–17. [CrossRef]
50. De Munshi, D.; Dutta, T.; Rebhi, R.; Mukherjee, M. Precision measurement of branching fractions of $^{138}Ba^{+}$: Testing many-body theories below the 1% level. *Phys. Rev. A* **2015**, *91*, 040501. [CrossRef]
51. Dutta, T.; de Munshi, D.; Yum, D.; Rebhi, R.; Mukherjee, M. An exacting transition probability measurement—A direct test of atomic many-body theories. *Sci. Rep.* **2016**, *6*, 29772. [CrossRef]
52. Lawler, J.E.; Wickliffe, M.E.; den Hartog, E.A.; Sneden, C. Improved Laboratory Transition Parameters forEu II and Application to the Solar Europium Elemental and Isotopic Composition. *Astrophys. J.* **2001**, *563*, 1075–1088. [CrossRef]
53. Wendt, K.; Ahmad, S.A.; Buchinger, F.; Mueller, A.C.; Neugart, R.; Otten, E.W. Relativistic J-dependence of the isotope shift in the 6s-6p doublet of Ba II. *Z. Phys. A Hadron. Nucl.* **1984**, *318*, 125–129. [CrossRef]
54. Hühnermann, H.; Möller, W.; Alkhazov, G.; Panteleev, V. Hyperfine-structure anomaly, its determination solely from A-factors, and nuclear moments of europium nuclei. *Inst. Phys. Conf. Ser.* **1992**, *132*, 209–211.
55. Möller, W.; Hühnermann, H.; Alkhazov, G.; Panteleev, V. How accurate are the "muonic" quadrupole moments in Eu? *Phys. Rev. Lett.* **1993**, *70*, 541–543. [CrossRef]
56. Revalde, G.; Enders, K.; Stachowska, E.; Marx, G.; Zolch, C.; Dembcynski, J.; Werth, G. Measurements of Hyperfine Structure of Stable and Instable Eu+ in a Paul Trap. *Laser Phys.* **1998**, *8*, 657–663.
57. Tsymbal, V.; Ryabchikova, T.; Sitnova, T. Software for NLTE Spectrum Fitting. In *Proceedings of the Physics of Magnetic Stars*; Astronomical Society of the Pacific Conference Series; Kudryavtsev, D.O., Romanyuk, I.I., Yakunin, I.A., Eds.; Astronomical Society of the Pacific: San Francisco, CA, USA, 2019; Volume 518, pp. 247–252.
58. Kochukhov, O. BinMag: Widget for Comparing Stellar Observed with Theoretical Spectra. 2018. https://ui.adsabs.harvard.edu/abs/2018ascl.soft05015K/abstract (accessed on 28 April 2026).
59. Butler, K.; Giddings, J. *Newsletter on the Analysis of Astronomical Spectra*; No. 9; University of London: London, 1985.
60. Mashonkina, L.I.; Belyaev, A.K. Even-to-Odd Barium Isotope Ratio in Selected Galactic Halo Stars. *Astron. Lett.* **2019**, *45*, 341–352. [CrossRef]
61. Mashonkina, L.; Gehren, T. Barium and europium abundances in cool dwarf stars and nucleosynthesis of heavy elements. *Astron. Astrophys.* **2000**, *364*, 249–264.
62. Storm, N.; Barklem, P.S.; Yakovleva, S.A.; Belyaev, A.K.; Palmeri, P.; Quinet, P.; Lodders, K.; Bergemann, M.; Hoppe, R. 3D NLTE modelling of Y and Eu. Centre-to-limb variation and solar abundances. *Astron. Astrophys.* **2024**, *683*, A200. [CrossRef]
63. Gustafsson, B.; Edvardsson, B.; Eriksson, K.; Jørgensen, U.G.; Nordlund, Å.; Plez, B. A grid of MARCS model atmospheres for late-type stars. I. Methods and general properties. *Astron. Astrophys.* **2008**, *486*, 951–970. [CrossRef]
64. Cowley, C.R.; Frey, M. Hyperfine Structure in the Barium Resonance Line: Curves of Growth for Solar and r-Process Isotopic Mixtures. *Astrophys. J.* **1989**, *346*, 1030. [CrossRef]
65. Mashonkina, L.; Gehren, T.; Bikmaev, I. Barium abundances in cool dwarf stars as a constraint to s- and r-process nucleosynthesis. *Astron. Astrophys.* **1999**, *343*, 519–530.
66. Mashonkina, L.; Zhao, G. Barium even-to-odd isotope abundance ratios in thick disk and thin disk stars. *Astron. Astrophys.* **2006**, *456*, 313–321. [CrossRef]
67. Mashonkina, L.; Zhao, G.; Gehren, T.; Aoki, W.; Bergemann, M.; Noguchi, K.; Shi, J.R.; Takada-Hidai, M.; Zhang, H.W. Non-LTE line formation for heavy elements in four very metal-poor stars. *Astron. Astrophys.* **2008**, *478*, 529–541. [CrossRef]
68. Sitnova, T.M.; Lombardo, L.; Mashonkina, L.I.; Rizzuti, F.; Cescutti, G.; Hansen, C.J.; Bonifacio, P.; Caffau, E.; Koch-Hansen, A.; Meynet, G.; et al. Unlocking the mystery of strontium synthesis in the early Galaxy through analysis of barium isotopes in very metal-poor stars. *Astron. Astrophys.* **2025**, *699*, A262. [CrossRef]
69. Jablonka, P.; North, P.; Mashonkina, L.; Hill, V.; Revaz, Y.; Shetrone, M.; Starkenburg, E.; Irwin, M.; Tolstoy, E.; Battaglia, G.; et al. The early days of the Sculptor dwarf spheroidal galaxy. *Astron. Astrophys.* **2015**, *583*, A67. [CrossRef]
70. Lodders, K. Relative Atomic Solar System Abundances, Mass Fractions, and Atomic Masses of the Elements and Their Isotopes, Composition of the Solar Photosphere, and Compositions of the Major Chondritic Meteorite Groups. *Space Sci. Rev.* **2021**, *217*, 44. [CrossRef]
71. Lugaro, M.; Karakas, A.I.; Stancliffe, R.J.; Rijs, C. The s-process in Asymptotic Giant Branch Stars of Low Metallicity and the Composition of Carbon-enhanced Metal-poor Stars. *Astrophys. J.* **2012**, *747*, 2. [CrossRef]

Disclaimer/Publisher's Note: The statements, opinions and data contained in all publications are solely those of the individual author(s) and contributor(s) and not of MDPI and/or the editor(s). MDPI and/or the editor(s) disclaim responsibility for any injury to people or property resulting from any ideas, methods, instructions or products referred to in the content.